

# Analysis of Numerical Simulation Database for Pressure Fluctuations Induced by High-Speed Turbulent Boundary Layers

Lian Duan\*

*Missouri University of Science and Technology, Rolla, MO 65409*

Meelan M. Choudhari†

*NASA Langley Research Center, Hampton, VA 23681*

Direct numerical simulations (DNS) of Mach 6 turbulent boundary layer with nominal freestream Mach number of 6 and Reynolds number of  $Re_\tau \approx 460$  are conducted at two wall temperatures ( $T_w/T_r = 0.25, 0.76$ ) to investigate the generated pressure fluctuations and their dependence on wall temperature. Simulations indicate that the influence of wall temperature on pressure fluctuations is largely limited to the near-wall region, with the characteristics of wall-pressure fluctuations showing a strong temperature dependence. Wall temperature has little influence on the propagation speed of the freestream pressure signal. The freestream radiation intensity compares well between wall-temperature cases when normalized by the local wall shear; the propagation speed of the freestream pressure signal and the orientation of the radiation wave front show little dependence on the wall temperature.

## Nomenclature

$C_p$	heat capacity at constant pressure, J/(K·kg)
$C_{pp}$	Space-time correlation coefficient of the pressure field, dimensionless
$C_v$	heat capacity at constant volume, J/(K·kg)
$H$	shape factor, $H = \delta^*/\theta$ , dimensionless
$M$	Mach number, dimensionless
$M_r$	relative Mach number, $M_r = (U_\infty - U_s)/a_\infty$ , dimensionless
$Pr$	Prandtl number, $Pr = 0.71$ , dimensionless
$R$	ideal gas constant, $R = 287$ , J/(K·kg)
$Re_\theta$	Reynolds number based on momentum thickness and freestream viscosity, $Re_\theta \equiv \frac{\rho_\infty U_\infty \theta}{\mu_\infty}$ , dimensionless
$Re_{\delta_2}$	Reynolds number based on momentum thickness and wall viscosity, $Re_{\delta_2} \equiv \frac{\rho_\infty U_\infty \theta}{\mu_w}$ , dimensionless
$Re_\tau$	Reynolds number based on shear velocity and wall viscosity, $Re_\tau \equiv \frac{\rho_w u_\tau \delta}{\mu_w}$ , dimensionless
$T$	temperature, K
$T_r$	recovery temperature, $T_r = T_\infty(1 + 0.9 * \frac{\gamma-1}{2} M_\infty^2)$ , K
$U_b$	bulk convection speed of pressure-carrying eddies, m/s
$U_s$	convection speed of ‘effective’ radiation sources, m/s
$U_\infty$	freestream velocity, m/s
$a$	speed of sound, m/s
$p$	pressure, Pa
$q$	dynamic pressure, Pa
$s$	entropy, J/K
$u$	streamwise velocity, m/s

---

\*Assistant Professor, Member, AIAA

†Aerospace Technologist, Computational AeroSciences Branch, M.S. 128. Associate Fellow, AIAA

$u_\tau$	friction velocity, m/s
$v$	spanwise velocity, m/s
$w$	wall-normal velocity, m/s
$x$	streamwise direction of the right-hand Cartesian coordinate
$y$	spanwise direction of the right-hand Cartesian coordinate
$z$	wall-normal direction of the right-hand Cartesian coordinate
$z_\tau$	viscous length, $z_\tau = \nu_w/u_\tau$ , m
$\gamma$	specific heat ratio, $\gamma = C_p/C_v$ , dimensionless
$\delta$	boundary layer thickness, m
$\delta^*$	displacement thickness, m
$\kappa$	thermal conductivity, $\kappa = \mu C_p/Pr$ , W/(m·K)
$\theta$	momentum thickness, m
$\mu$	dynamic viscosity, $\mu = 1.458 \times 10^{-6} \frac{T^{3/2}}{T+110.4}$ , kg/(m·s)
$\nu$	kinematic viscosity, $\nu = \mu/\rho$ , m <sup>2</sup> ·s
$\rho$	density, kg/m <sup>3</sup>
$\omega$	frequency, rad/s
$\Omega$	vorticity, s <sup>-1</sup>

### Subscripts

$i$	inflow station for the domain of direct numerical simulations
$rms$	root mean square
w	wall variables
$\infty$	freestream variables
$t$	stagnation quantities

### Superscripts

$+$	inner wall units
$\overline{(\cdot)}$	averaged variables
$(\cdot)'$	perturbation from averaged variable

## I. Introduction

Prediction of laminar-turbulent transition is a critical part of the design of hypersonic vehicles because of the large increase in skin-friction drag and surface heating associated with the onset of transition. Despite continued advances in transition research, the physics of boundary layer transition over these vehicles is not fully understood due to the lack of detailed experimental measurements. Transition testing in conventional (i.e., noisy) wind tunnels has been an important avenue to understanding the transition behavior of hypersonic vehicles, despite the common knowledge that conventional wind-tunnel facilities cannot reliably simulate the in-flight transition behavior over a smooth surface due to the effects of the elevated levels of freestream disturbances.<sup>1-3</sup> Recent evidence suggests that freestream disturbances may also influence the accelerated onset of transition caused by isolated roughness elements on a nominally smooth surface.<sup>4</sup> Transition measurements in low disturbance (i.e., quiet) wind tunnels better mimic the in-flight transition characteristics. However, because of the size and Reynolds number limitations of the existing quiet facilities, conventional tunnels will continue to be employed for the testing and evaluation of hypersonic vehicles, especially during ground tests involving large-scale models.

Facility disturbances in conventional tunnels can impact not only the transition location but, possibly, the transition mechanism as well. As a result, the existing methodology to extrapolate wind-tunnel transition results to flight is rather crude and requires substantial improvement. To enable more effective use of the transition data from conventional facilities and permit more accurate extrapolation of the wind-tunnel results to flight, an in-depth knowledge of the broadband disturbance environment in those facilities must be developed.

In unheated tunnels with adequate flow conditioning, the acoustic disturbances are likely to dominate the overall disturbance environment at Mach numbers of 2.5 or above,<sup>5-7</sup> and their effect on transition

cannot be quantified in terms of a single metric corresponding to the root-mean-square amplitude of the freestream disturbances as indicated by the measurements at Purdue University.<sup>3</sup> With the exception of the early measurements of freestream pressure fluctuations by Laufer<sup>5</sup> and a few others,<sup>2,8</sup> there are few measurements that are detailed enough to be suitable for either comparing with computational predictions or for developing models that can be used towards more reliable transition models. The measurements are typically susceptible to experimental errors due to the poor spatial resolution and/or limited frequency response of pressure transducers.<sup>9</sup> Theoretical models for acoustic radiation from a supersonic boundary layer were developed by Phillips<sup>10</sup> and Ffowcs-Williams and Maidanik,<sup>11</sup> which attributed a major cause of the acoustic radiation to eddy Mach waves from boundary-layer turbulence convecting supersonically with respect to the freestream. However, a lack of adequate knowledge concerning the boundary-layer turbulence restricted the theoretical predictions to the intensity of the freestream acoustic fluctuations alone.

Direct Numerical Simulation (DNS) is a valuable tool that can overcome some of the aforementioned difficulties with both experimental measurements and theory and, hence, provide access to both flow and acoustic quantities that are difficult to obtain otherwise. The DNS can also isolate the acoustic radiation due to individual physical mechanisms, thereby avoiding any contamination due to secondary sources such as vortical and entropy fluctuations in the incoming stream.

The successful application of DNS in capturing the freestream acoustic pressure fluctuations has been demonstrated for Mach 2.5 and Mach 6 boundary layers by the present authors.<sup>12–14</sup> Single and multi-point statistics of the computed freestream pressure fluctuations were reported, including the intensity, frequency spectra, space-time correlations, and convection velocities. However, a comprehensive understanding of the freestream disturbance field and its dependence of boundary-layer parameters (e.g., freestream Mach number, wall temperature, and Reynolds number) is still lacking. The current study focuses on exploring the dependence of boundary-layer induced pressure fluctuations on wall temperature at hypersonic speeds. A new DNS dataset at Mach 6 with a different wall temperature than the previous Mach 6 data<sup>13</sup> is introduced for the study of wall-temperature effects.

The paper is organized as follows. The flow conditions selected for the numerical simulation of hypersonic turbulent boundary layers and the numerical method used for these simulations are outlined in Section II. Section III is focused on an analysis of freestream pressure fluctuations, highlighting their dependence on the wall temperature. conclusions thus far are outlined in Section IV.

## II. Simulation details

### A. Flow conditions and numerical methodology

Table 1 outlines the freestream flow condition for the present simulations. The freestream condition is similar to the operational conditions of the Boeing/AFOSR Mach-6 Quiet Tunnel<sup>3,4</sup> (BAM6QT) under noisy flow conditions with a total pressure of 921 kPa and a total temperature of 433 K. Table 2 lists the values of the mean boundary layer parameters at the selected downstream location for statistical analysis ( $x_a = 57\delta_i$  for Case M6Tw076 and  $x_a = 80\delta_i$  for Case M6Tw025). The wall temperature for Case M6Tw076 is similar to that at the nozzle wall of BAM6QT, corresponding to a wall temperature ratio of  $T_w/T_r \approx 0.76$ . Case M6Tw025 has the same freestream conditions and Reynolds number,  $Re_\tau$ , as Case M6Tw076 but a lower wall temperature ( $T_w/T_r \approx 0.25$ ). Thus, by comparing the results of Cases M6Tw025 and M6Tw076, the effect of wall cooling on the pressure fluctuations can be investigated at a fixed Reynolds number  $Re_\tau$ . When necessary, the results of the two Mach 6 cases will be compared with a Mach 2.5 DNS case<sup>14</sup> to highlight the effect of freestream Mach number.

The details of the DNS methodology, including numerical methods, initial and boundary conditions, have been documented in our previous papers.<sup>13,14</sup> Figure 1 shows the general computational set-up for Case M6Tw025. The computational set-up of Case M6Tw076 parallels that of Case M6Tw025. The inflow boundary condition is prescribed by means of a recycling-rescaling method and the selected rescaling length is sufficiently large to accommodate the eddy decorrelation length and minimize any spurious correlation in boundary layer fluctuations as a result of the recycling process.<sup>14</sup> Figures 3a and 3b show that the pressure fluctuations both at the wall and in the freestream for Case M6Tw025 have become homogeneous in the streamwise direction after  $x/\delta_i = 55$ , indicating that both the boundary-layer turbulence and the freestream acoustic field have gone through the transient adjustment due to recycled inflow and reestablished equilibrium at the selected downstream location for statistical analysis. The streamwise variations of relevant quantities such as  $C_f$ ,  $\delta$ , and rms pressure fluctuations at the wall and in the free stream are also used to gauge the

extent of the transient region.

In the following section, averages are first calculated over a streamwise window of  $[x_a - 0.9\delta_i, x_a + 0.9\delta_i]$  ( $x_a = 80\delta_i$  for Case M6Tw025 and  $x_a = 55\delta_i$  for Case M6Tw076) and spanwise locations for each instantaneous flow field; then, an ensemble average over flow field snapshots spanning a time interval of approximately  $240\delta_i/U_\infty$  is calculated. To monitor the statistical convergence, flow statistics are computed by averaging over the whole or half the number of the flow-field snapshots and negligible difference ( $< 1\%$ ) is observed between the two.

Power spectra are calculated using the Welch method<sup>15</sup> with 8 segments and 50% overlap. A Hamming window is used for weighting the data prior to the fast Fourier transform (FFT) processing. The sampling frequency is approximately  $63U_\infty/\delta_i$ , or 4 MHz, and the length of an individual segment is approximately  $53.2\delta_i/U_\infty$ . Negligible difference in spectral estimation is observed within the reported frequency range, when the overall time record is subdivided in 12 segments instead of the baseline number of 8 segments. In addition, the DNS methodology has been extensively validated in previous work for supersonic/hypersonic turbulent boundary layers<sup>16–19</sup> and for supersonic shock wave-turbulent boundary layer interactions.<sup>20–22</sup>

## B. Domain/grid sensitivity assessment

In this section, the dependence of numerical results on the domain size and grid resolution for Case M6Tw076 is investigated by a series of auxiliary DNS simulations listed in Table 3 where Case M6Tw076 is the baseline simulation and cases AI and AII are two auxiliary DNS simulations for Case M6Tw076. All cases are identical in terms of numerical method, computational set-up, and flow conditions except for the parameters listed in the table. In particular, Case AI has the same grid resolution as the baseline case but only two-fifths of the spanwise domain size and 15% longer streamwise domain size, and Case AII has the same domain size as case AI but with 1.5 times higher grid resolution in each direction when compared with the other two cases. As a result, the effects of streamwise and spanwise domain sizes can be investigated by comparing the results of the baseline case and AI, and the grid sensitivity can be demonstrated by comparing the differences between cases AI and AII. Furthermore, the effectiveness of the outflow boundary condition can be assessed by comparing the solutions near the outflow boundary for the baseline case and case AI.

Figure 4a plots the intensity of pressure fluctuation across the boundary layer for DNS solutions corresponding to each of these three cases. All curves collapse to within 1%, indicating that the single point statistics of most interest are insensitive to the spanwise domain size and the grid resolution. To further ascertain the dependence of high-frequency spectral components on the grid resolution, Figures 4b and 4c compare the frequency spectrum of pressure fluctuations at the wall and in the free stream, respectively, for the three simulations at the station selected for statistical analysis (Table 2). Good agreement is achieved up to  $\omega\delta/U_\infty \approx 25$  or equivalently for  $\omega\nu_w/u_\tau^2 \approx 1$ . The under-resolved frequency range ( $\omega\delta/U_\infty > 25$ ) contains less than 0.4% of the total energy and the pressure spectra in compensated form (not shown here) for the three cases are indistinguishable from each other over the range of resolved frequencies.

To further assess the accuracy of the numerical scheme for resolving the propagation of acoustic disturbances in the free stream, we note that the maximum frequency resolved by the streamwise grid spacing of  $\Delta x$  (note that the  $\Delta x > \Delta y > \Delta z$ ) may also be estimated as:

$$\omega_{max} = \frac{2\pi U_c}{n\Delta x} \quad (1)$$

where  $U_c$  refers to the streamwise propagation speed of the acoustic disturbance, and  $n$  denotes the minimum number of points per wavelength required for an algorithm to provide desired accuracy. Based on previous findings that the employed Weighted Essentially Non-Oscillatory (WENO) scheme can achieve a resolution of  $n = 8$  PPW,<sup>23</sup> and setting  $U_c/U_\infty = 0.7$  based on the results presented in Section D, the spatial resolution is deemed to be adequate up to  $\omega_{max}\delta/U_\infty \approx 25$ . The latter bound approximately coincides with the frequency at which the differences between cases AI and AII begin to appear.

Similar assessments for domain size and the grid resolution are conducted for Case M6Tw025, and good frequency bandwidth is achieved up to  $\omega_{max}\delta/U_\infty \approx 25$ .<sup>14</sup> Additional evidence to demonstrate satisfactory numerical accuracy of the current simulation is presented in the following sections, wherein the computed flow statistics are compared with both experiments and other high-quality simulations at similar flow conditions.

## C. Comparison with experiments

In this section, we demonstrate the accuracy of the current simulation by comparing the computed flow statistics with experiments at similar flow conditions. Figure 5 shows the comparison of DNS results (Case M6Tw076) with the wind-tunnel measurement and the calculation using Harris Boundary-layer code<sup>24</sup> conducted by Katya Casper for a Mach 5.8 turbulent boundary layer on the nozzle wall of BAM6QT under noisy-flow conditions ( $Re = 9.69 \times 10^6/m$ ,  $P_{t,\infty} = 965$  kPa,  $T_{t,\infty} = 429$  K). The DNS and experiments agree well with each other in terms of both boundary-layer profile and wall-pressure spectrum. In comparison, the Mach number profile based on the boundary layer code exhibits larger differences from the measurement and the DNS in the outer part of the boundary layer. Moreover, Figure 5c and Figure 5d show that DNS successfully extends the measured spectra to higher frequencies. The resolution of the high-frequency region as well as the acoustic radiation due to these high-frequency fluctuations are especially important for studying the receptivity process associated with second-mode waves in hypersonic wind tunnels.

Additional comparisons of DNS results with both experiments and other high-quality simulations are presented in the following sections.

## III. Results

In this section, the effects of wall temperature on the pressure fluctuations induced by hypersonic turbulent boundary layers are investigated by comparing results between Case M6Tw025 and Case M6Tw076.

### A. Boundary layer statistics

Next, turbulence statistics across the boundary layer are plotted and compared with well-established empirical correlations and numerical data sets.

The van Driest transformed mean velocity profile based on the DNS is shown in Figure 6a. The mean velocity conforms well to the incompressible law-of-the-wall upon van Driest transformation and shows a (narrow) logarithmic region. In addition, the mean-velocity profile compares well with the experimental results by Bookey et al.<sup>25</sup> at Mach 2.9,  $Re_\tau = 501$  and the recent DNS results by Pirozzoli and Bernardini<sup>26</sup> at Mach 2,  $Re_\tau = 497$ .

Figure 7 shows that wall cooling has a significant influence on  $p'_{rms}/\tau_w$  in the near-wall region ( $z^+ < 150$ ), with  $p'_{w,rms}/\tau_w \approx 3.4$  for Case M6Tw025 and  $p'_{w,rms}/\tau_w \approx 2.6$  for Case M6Tw076, indicating an increase of approximately 30 percent in the cold-wall case. The pressure fluctuations have a rapid gradient near the wall for the cold-wall case, so that a portion of the pressure fluctuations damps out across the buffer layer. The influence of wall cooling becomes much weaker in the outer part of the boundary layer ( $z^+ > 150$ ) and nearly vanishes in the free stream. Outside the boundary layer,  $p'_{rms}/\tau_w$  approaches a constant value of about 0.86 for the both Mach 6 cases.

In terms of the influence of freestream Mach number,  $p'_{rms}/\tau_w$  shows only a weak Mach-number dependence within the boundary layer, consistent with previous findings.<sup>13,27</sup> However, it exhibits a strong Mach-number dependence in the free stream. The variation of freestream value with Mach number is consistent with the trend predicted by the experimental data reported by Laufer<sup>5</sup> (Figure 8).

Similar to the pressure rms, the rms values of fluctuating velocity components ( $u'_{rms}$ ,  $v'_{rms}$ ,  $w'_{rms}$ ) and other thermodynamic quantities ( $\rho'_{rms}$ ,  $T'_{rms}$ ) also reach non-zero, nearly constant values within the free stream (at least up to  $z = 5\delta$  before the computational grid becomes significantly coarser). The constant asymptotes within the freestream indicate that local homogeneity in the wall-normal direction is established for all freestream disturbances, at least in terms of their rms amplitudes.

### B. Characteristics of freestream fluctuations

The characteristics of freestream fluctuations will now be analyzed using the theory of modal analysis, which was initially proposed by Kovasznay<sup>28</sup> and further developed by Logan<sup>29</sup> and Smits and Dussauge.<sup>30</sup> According to Kovasznay,<sup>28</sup> the fluctuations at any point within a uniform mean flow can be represented as a superposition of three different modes with co-varying physical properties: the vorticity mode, the acoustic or sound-wave mode and the entropy mode (also referred to as entropy spottiness or temperature spottiness). Modal analysis has been used by a number of experimental researchers to characterize the freestream disturbance environment in their facilities. Examples include Donaldson and Coulter<sup>2</sup> who evaluated the level

and the sources of disturbances in the Arnold Engineering Development Center (AEDC) Tunnels A and B, Weiss et al.<sup>31</sup> who used a specially designed constant temperature anemometer to map out the freestream disturbance field within a Mach 2.54 short duration supersonic facility at Stuttgart University, and Masutti et al.<sup>32</sup> who characterized the freestream fluctuations in the Mach 6 Hypersonic Wind Tunnel H3 of the von Karman Institute.

Table 4 and Table 5 list the freestream values of several fluctuating flow variables for Cases M6Tw025 and M6Tw076, respectively. Here,  $s$  is specific entropy,  $\Omega$  is the vorticity, and the subscript ‘t’ denotes stagnation quantities. A comparison of the data from these two tables indicates that the magnitude of freestream fluctuations normalized by the respective mean values increase significantly as the wall temperature decreases, including both the velocity fluctuations and the fluctuations in thermodynamic variables. In particular, the pressure fluctuations in the free stream, including  $p'_{rms}/\bar{p}$  and  $p'_{t,rms}/\bar{p}_t$ , are considerably different for both cases (3.52% vs 2.01% for  $p'_{rms}/\bar{p}$ , 1.13% vs 0.648% for  $p'_{t,rms}/\bar{p}_t$ , larger value for the cold-wall case). However,  $p'_{rms}/\bar{p}$  and  $p'_{t,rms}/\bar{p}_t$  bear nearly the same ratio of about 1.8 across the two cases. For both wall-temperature cases, the variation in rms amplitudes of velocity fluctuations along the three Cartesian axes indicates the anisotropy of the freestream velocity fluctuations, with the wall-normal velocity fluctuations the largest in the freestream. The relative perturbations in thermodynamic variables are nearly an order of magnitude larger than the velocity fluctuations. Consequently, the mass-flux fluctuations in the freestream are dominated by the density fluctuations, similar to the findings in the Mach 2.5 supersonic boundary layer.<sup>14</sup> Also observe that  $u'$  and  $p'$  are not perfectly anti-correlated for either case, which is assumed by Laufer<sup>5</sup> in analyzing his hot-wire data. The negative correlation between  $u'$  and  $p'$  becomes stronger in the cold-wall case ( $-0.845$  vs  $-0.632$ ).

The fact that  $s'_{rms}/R \ll p'_{rms}/\bar{p}$  confirms the negligible contribution of entropy mode to the overall freestream disturbance. The pressure fluctuation in the freestream is nearly perfectly correlated with the fluctuations in density and temperature, so that the fluctuations in thermodynamic quantities satisfy the following isentropic relations

$$\frac{T'_{rms}}{\bar{T}} \approx \frac{\gamma - 1}{\gamma} \frac{p'_{rms}}{\bar{p}} \quad (2)$$

$$\frac{\rho'_{rms}}{\bar{\rho}} \approx \frac{1}{\gamma} \frac{p'_{rms}}{\bar{p}} \quad (3)$$

analogous to purely acoustic disturbances. The correlation between the fluctuations in pressure and velocity is also strong, but significantly less than unity. The near zero correlation between pressure and spanwise velocity fluctuations is a consequence of spanwise homogeneity and simply confirms the satisfactory convergence of the statistical estimates. The relative importance of the acoustic and vorticity modes in the freestream can be assessed via the ratio of the dilatation variance  $(\partial u_i / \partial x_i)^2$  and the vorticity variance  $\overline{\Omega'_i \Omega'_i}$  in the freestream. These variances are representative of the disturbance energy in the acoustic and vorticity modes, respectively, and the large value of  $(\partial u_i / \partial x_i)^2 / \overline{\Omega'_i \Omega'_i}$  implies the overwhelming dominance of acoustic mode over the vorticity mode in the free stream.

The dominance of the acoustic mode over the other two modes confirms that a purely acoustic field in the free stream is successfully isolated by the present DNS. In typical high-speed (noisy) wind tunnels, however, freestream disturbances may originate from multiple disturbances sources (screens, heat exchangers, valves, bends, diffusers, and compressors upstream of the test section and vibration, roughness and waviness, boundary layer transition, and model-wall interference within the test section) and while acoustic disturbances may still be dominant, all three modes contribute to the freestream fluctuations in general.<sup>2,31-33</sup> In that regard, the present simulation provides a more controlled setting for studying the spectral features and production mechanisms specific to the acoustic disturbance environment resulting from turbulent tunnel wall boundary layers.

### C. Frequency spectra of pressure fluctuations

Figure 9 shows the comparison of frequency spectra at the wall and in the free stream for Cases M6Tw025 and M6Tw076. The wall-pressure spectrum shows a strong wall temperature dependence, which scales neither in outer variables (Figure 9a) nor in inner variables (Figure 9a). Figure 10a shows that the pre-multiplied wall-pressure spectrum for Case M6Tw025 consists of a sharper peak with a faster roll-off at high frequencies compared with Case M6Tw076, and wall cooling causes a shift in the dominant frequency from  $\omega \delta / U_\infty \approx 9$  for Case M6Tw076 to  $\omega \delta / U_\infty \approx 15$  for Case M6Tw025.

For the freestream pressure spectrum, Figure 9c shows that the low-frequency range of  $\phi_p(\omega)$  scales in outer variables; and Figure 9d shows that the high-frequency range scales in inner-variable scales, which conforms to the findings of wall-pressure spectrum in low-speed adiabatic flows.<sup>34</sup> Moreover, Figure 10b shows that the dominant frequency of freestream pressure spectrum is independent of wall temperature, indicating insignificant influence of wall cooling on the freestream pressure spectrum.

#### D. Space-time correlation and propagation speed

The statistical properties of the pressure field are investigated through the space-time correlation coefficient defined as

$$C_{pp}(\Delta x, \Delta y, \Delta t) = \frac{\overline{p'(x, y, z, t)p'(x + \Delta x, y + \Delta y, z, t + \Delta t)}}{\left(\overline{p'^2(x, y, z, t)}\right)^{1/2} \left(\overline{p'^2(x + \Delta x, y + \Delta y, z, t + \Delta t)}\right)^{1/2}} \quad (4)$$

where  $\Delta x$  and  $\Delta y$  are spatial separations in the streamwise and spanwise directions, respectively, and  $\Delta t$  is the time delay.

The space-time correlation contours  $C_{pp}(\Delta x, 0, \Delta t)$  of the surface and freestream pressure fluctuations are shown in figures 11a and 11b, respectively, for Cases M6Tw025 and M6Tw076. The skewed shape of the contours at both locations indicates the convective nature of the pressure field, which is characterized by downstream propagation of either the coherent pressure-carrying eddies within the boundary layer or the pressure wavepackets in the free stream. The similar inclination of the space-time correlation contours in the free stream between Cases M6Tw025 and M6Tw076 indicates that wall cooling has almost no influence on the overall propagation speed of radiated pressure wavepackets in the free stream.

To quantitatively represent the overall propagation speed of pressure-carrying eddies or wavepackets, the bulk propagating speed ( $U_b$ ) is defined as the one that minimizes the difference between the real time evolution of  $p(x, t)$  and a frozen wave  $p(x - U_b t)$ . Following this definition, the following expression can be obtained

$$U_b \equiv -\frac{(\partial p / \partial t)(\partial p / \partial x)}{(\partial p / \partial x)^2} \quad (5)$$

The same definition of bulk propagation speed was introduced by Del Alamo<sup>35</sup> for the streamwise velocity fluctuations.

Figure 12 plots the bulk propagation speed of the pressure fluctuation as a function of wall-normal distance. It is shown that wall cooling decreases the convection speed of pressure-carrying eddies within the boundary layer but has nearly no influence on the propagation speed of radiated pressure wavepackets in the free stream, where the bulk propagation speed is approximately  $0.7U_\infty$  for both wall-temperature cases.

Figure 12 further shows that for both cases, the bulk propagation speed of the pressure fluctuation is larger than the local mean velocity near the wall and becomes smaller than the mean velocity farther away from the wall, which is consistent with previous findings.<sup>13,14,27,36</sup> The convection speed of pressure-carrying eddies is larger than the local mean velocity over a significant portion of boundary layer (up to  $z/\delta \approx 0.65$ ) for Case M6Tw076 while the analogous region is much smaller for the colder wall case (Case M6Tw025). The region where  $\bar{u} \approx U_b$  seems to be limited to the upper buffer layer and the log layer, at least for the present study.

The value of convection/propagation speed is known to vary depending on specific definitions.<sup>37</sup> Thus, further comparison with different definitions of the convection speed over a wider range of flow conditions is required to confirm the above observations. Also, it is well known that the propagation/convection speed of turbulent eddies is a function of temporal frequency and spatial wave numbers,<sup>35,36</sup> and further study is necessary to characterize the influence of wall cooling on the frequency- and wave-number dependence of the convection speed.

Figures 13a and 13b show the variation of bulk convection speed with freestream Mach number at the wall and in the free stream, respectively. While the data by Kistler & Chen<sup>38</sup> shows that the convection speed at the wall plateaus for  $M_\infty > 2$ , the current DNS and the data reported by Bernadini and Pirozzoli<sup>27</sup> and Duan et al.<sup>14</sup> show a weak increase with the freestream Mach number. Both the current DNS and the experimental measurements by Laufer<sup>5</sup> show that the bulk convection speed in the free stream increases with freestream Mach number. All the freestream bulk convection speeds fall within the region where  $M_r > 1$ , with  $M_r \equiv (U_\infty - U_b)/a_\infty$ , which supports the basic concept of ‘eddy Mach wave’ radiation<sup>10,11</sup> and shows

that the Mach-wave-type radiation is produced by eddies, which are convected supersonically with respect to the free stream.

### E. Wave-front orientation

In this section, the wave-front orientation of Mach-wave radiation is discussed, which is an important quantity from the standpoint of transition analysis, since the receptivity characteristics are known to be sensitive to the orientation of the plane-wave disturbance.<sup>39</sup>

Figure 14 shows that the instantaneous pressure field in the free stream for Cases M6Tw025 and M6Tw076. For both wall temperatures, the acoustic radiation consists of randomly spaced wavefronts, each with a limited spatial coherence. The wave fronts exhibit a preferred orientation within the streamwise–wall-normal ( $x$ - $z$ ) plane. By assuming purely plane-wave like radiation pattern, the wave-front orientation can be derived using the following acoustic relation<sup>40</sup>

$$\frac{u'_n}{U_\infty} = \frac{1}{\gamma M_\infty} \frac{p'}{p_\infty} \quad (6)$$

where  $u_n = \mathbf{u} \cdot \mathbf{n}$  is the velocity normal to the wave front and  $\mathbf{n} = (\cos\theta_n, \sin\theta_n)$  is the plane-wave normal direction. The wave-front orientation that is statistically most likely can be determined to be the direction that minimizes the difference between  $u'_{n,rms}/U_\infty$  and  $p'_{rms}/(\gamma M_\infty p_\infty)$ . By using the freestream statistics analogous to Tables 5 and 4),  $\theta_n \approx 120^\circ$  (correspondingly the angle between the wave front and the flow direction  $\theta = 30^\circ$ ) is obtained for both cases, which agrees with the approximate inclination of the wave fronts from the numerical schlieren image in figure 14. Laufer<sup>5</sup> has used a similar but less rigorous relation  $u'_n \cos\theta_n = u'$  to estimate the wave-orientation, since the streamwise velocity fluctuation  $u'$  is the only velocity component that could be measured in his experiments.

The reader should note that the freestream acoustic field does not correspond to truly planar waves as indicated by the instantaneous pressure field in the spanwise–wall-normal ( $y$ - $z$ ) plane for both cases. The deviation from purely planar behavior is also evident in a statistical sense from the imperfect correlation between  $p'$  and the streamwise ( $u'$ ) and wall-normal ( $w'$ ) velocity fluctuations in the freestream region. (Recall the data presented in Tables 5 and 4). The finite spanwise extent of the pressure wavepackets is consistent with the finite size of acoustic sources that are responsible for generating the waves.

While the overall orientation of the acoustic radiation for Cases M6Tw025 and M6Tw076 is nearly the same ( $\theta \approx 30^\circ$ ), the wavepackets of the radiation field for Case M6Tw025 are more spatially coherent compared with Case M6Tw076, as indicated by the larger spatial extent of the radiated wavefronts in the numerical schlieren image. Such an increase in spatial coherence for Case M6Tw025 is consistent with the larger correlations between  $p'$  and ( $u'$ )- and ( $w'$ )-velocity fluctuations. The increased coherence of radiated wavepackets with wall cooling may be a result of increased coherence of near-wall turbulent structures due to wall cooling,<sup>17</sup> as the acoustic sources that can directly radiate to the free stream are associated with eddies with  $M_r > 1$ , and, hence, are confined to the near-wall region of the boundary layer. Detailed analysis of the structural characteristics of the acoustic sources is still necessary to confirm this argument.

## IV. Conclusion

DNS of Mach 6 turbulent boundary layers with two different wall temperatures ( $T_w/T_r = 0.25, 0.76$ ) are conducted to investigate the effect of wall temperature on the pressure fluctuations generated by hypersonic boundary layers. Simulations show that wall cooling significantly modifies the pressure-fluctuation intensities near the wall, with  $p'_{w,rms}/\tau_w$  varying from 2.6 for  $T_w/T_r = 0.76$  to 3.4 for  $T_w/T_r = 0.25$ . Furthermore, the frequency spectra of wall-pressure fluctuations for the two cases show considerable differences when plotted in terms of either outer-layer or inner-layer variables. The peak of the pre-multiplied spectrum shifts to a higher value as the wall temperature decreases.

In terms of the freestream pressure fluctuations, although the radiation intensity shows a strong wall-temperature dependence when normalized by the mean freestream pressure ( $\bar{p}_\infty$ ), the radiation intensity compares well between the two cases when normalized by the local wall shear. Wall cooling increases the spatial correlation of the freestream pressure field, but has little influence on the frequency spectrum, the propagation speed, or the dominant orientation of the radiation wave fronts.



## Acknowledgments

This material is based on the work supported by National Aeronautics and Space Administration, Langley Research Center under the Research Cooperative Agreement No. NNL09AA00A (subcontracted through the National Institute of Aerospace). The authors would like to thank Dr. Katya Casper for providing her wind-tunnel measurements for comparison with DNS. Prof. Pino Martín of the University of Maryland provided the original code which has been modified for the current study. The simulations have been conducted using the Pleiades Supercomputer of the NASA Advanced Supercomputing (NAS) Division and the Extreme Science and Engineering Discovery Environment (XSEDE), which is supported by National Science Foundation grant number OCI-1053575.

## References

- <sup>1</sup>Pate, S. R. and Schuller, C. J., “Radiated Aerodynamic Noise Effects on Boundary Layer Transition in Supersonic and Hypersonic Wind Tunnels,” *AIAA Journal*, Vol. 7, No. 3, 1969, pp. 450–457.
- <sup>2</sup>Donaldson, J. and Coulter, S., “A Review of Free-Stream Flow Fluctuation and Steady-State Flow Quality Measurements in the AEDC/VKF Supersonic Tunnel A and Hypersonic Tunnel B,” AIAA Paper 95-6137, 1995.
- <sup>3</sup>Schneider, S. P., “Effects of High-Speed Tunnel Noise on Laminar-Turbulent Transition,” *Journal of Spacecraft and Rockets*, Vol. 38, No. 3, 2001, pp. 323–333.
- <sup>4</sup>Borg, M. P. and Schneider, S. P., “Effect of Free-stream Noise on Roughness-Induced Transition for the X-51A Forebody,” *Journal of Spacecraft and Rockets*, Vol. 45, No. 6, 2008, pp. 1106–1116.
- <sup>5</sup>Laufer, J., “Some Statistical Properties of the Pressure Field Radiated by a Turbulent Boundary Layer,” *Physics of Fluids*, Vol. 7, No. 8, 1964, pp. 1191–1197.
- <sup>6</sup>Stetson, K. F., “Nosetip Bluntness Effects on Cone Frustum Boundary-Layer Transition in Hypersonic Flow,” AIAA Paper 83-1763, 1983.
- <sup>7</sup>Bushnell, D. M., “Notes on Initial Disturbance Fields for the Transition Problem,” *Instability and Transition*, edited by M. Y. Hussaini and R. G. Voigt, Springer-Verlag, Berlin, Vol. 1, 1990, pp. 217–232.
- <sup>8</sup>Kendall, J. M., “Supersonic Boundary Layer Transition Studies,” *Space Program Summary*, Vol. 3, 1970, pp. 43–47.
- <sup>9</sup>Beresh, S. J., Henfling, J. F., Spillers, R. W., and Pruett, B. O. M., “Fluctuating Wall Pressures Measured beneath a Supersonic Turbulent Boundary Layer,” *Physics of Fluids*, Vol. 23, No. 7, 2011, 075110.
- <sup>10</sup>Phillips, O. M., “On the Generation of Sound by Supersonic Turbulent Shear Layers,” *Journal of Fluid Mechanics*, Vol. 9, 1960, pp. 1–28.
- <sup>11</sup>Ffowcs-Williams, J. E. and Maidanik, G., “The Mach Wave Field Radiated by Supersonic Turbulent Shear Flows,” *Journal of Fluid Mechanics*, Vol. 21, 1965, pp. 641–657.
- <sup>12</sup>Duan, L., Choudhari, M., and Wu, M., “Numerical Study of Pressure Fluctuations Due to High-Speed Turbulent Boundary Layers,” AIAA Paper 2012-3070, 2012.
- <sup>13</sup>Duan, L. and Choudhari, M. M., “Numerical Study of Pressure Fluctuations due to a Mach 6 Turbulent Boundary Layer,” AIAA Paper 2013-0532, 2013.
- <sup>14</sup>Duan, L., Choudhari, M. M., and Wu, M., “Numerical Study of Acoustic Radiation due to a Supersonic Turbulent Boundary Layer,” *Journal of Fluid Mechanics*, Vol. 746, 2014, pp. 165–192.
- <sup>15</sup>Welch, P. D., “The Use of Fast Fourier Transform for the Estimation of Power Spectra: A Method Based on Time Averaging Over Short, Modified Periodograms,” *IEEE Trans. Audio Electroacoustics*, Vol. AU-15, 1967, pp. 70–73.
- <sup>16</sup>Martín, M., “DNS of Hypersonic Turbulent Boundary Layers. Part I: Initialization and Comparison with Experiments,” *Journal of Fluid Mechanics*, Vol. 570, 2007, pp. 347–364.
- <sup>17</sup>Duan, L., Beekman, I., and Martín, M. P., “Direct Numerical Simulation of Hypersonic Turbulent Boundary Layers. Part 2: Effect of Wall Temperature,” *Journal of Fluid Mechanics*, Vol. 655, 2010, pp. 419–445.
- <sup>18</sup>Duan, L., Beekman, I., and Martín, M. P., “Direct Numerical Simulation of Hypersonic Turbulent Boundary Layers. Part 3: Effect of Mach Number,” *Journal of Fluid Mechanics*, Vol. 672, 2011, pp. 245–267.
- <sup>19</sup>Duan, L. and Martín, M. P., “Direct Numerical Simulation of Hypersonic Turbulent Boundary Layers. Part 4: Effect of High Enthalpy,” *Journal of Fluid Mechanics*, Vol. 684, 2011, pp. 25–59.
- <sup>20</sup>Wu, M. and Martín, M. P., “Direct Numerical Simulation of Supersonic Boundary Layer over a Compression Ramp,” *AIAA Journal*, Vol. 45, No. 4, 2007, pp. 879–889.
- <sup>21</sup>Wu, M. and Martín, M. P., “Analysis of Shock Motion in Shock Wave and Turbulent Boundary Layer Interaction using Direct Numerical Simulation Data,” *Journal of Fluid Mechanics*, Vol. 594, 2008, pp. 71–83.
- <sup>22</sup>Priebe, S. and Martín, M. P., “Low-Frequency Unsteadiness in Shock Wave Turbulent Boundary Layer Interaction,” *Journal of Fluid Mechanics*, Vol. 699, 2012, pp. 1–49.
- <sup>23</sup>Taylor, E. M., Wu, M., and Martín, M. P., “Optimization of Nonlinear Error Sources for Weighted Non-Oscillatory Methods in Direct Numerical Simulations of Compressible Turbulence,” *Journal of Computational Physics*, Vol. 223, No. 1, 2006, pp. 384–397.
- <sup>24</sup>Harris, J. and Blanchard, D., “Computer Program for Solving Laminar, Transitional, or Turbulent Compressible Boundary-Layer Equations for Two-Dimensional and Axisymmetric Flow,” NASA-TM-83207, 1982.
- <sup>25</sup>Bookey, P., Wyckham, C., Smits, A. J., and Martin, M. P., “New Experimental Data of STBLI at DNS/LES Accessible Reynolds Numbers,” AIAA Paper 2005-309, 2005.

- <sup>26</sup>Pirozzoli, S. and Bernardini, M., “Turbulence in Supersonic Boundary Layers at Moderate Reynolds Numbers,” *Journal of Fluid Mechanics*, Vol. 688, 2011, pp. 120–168.
- <sup>27</sup>Bernardini, M. and Pirozzoli, S., “Wall Pressure Fluctuations beneath Supersonic Turbulent Boundary Layers,” *Physics of Fluids*, Vol. 23, No. 8, 2011, 085102.
- <sup>28</sup>Kovaszny, L. S. G., “Turbulence in Supersonic Flow,” *Journal of Aeronautical Sciences*, Vol. 20, 1953, pp. 657–674.
- <sup>29</sup>Logan, P., “Modal Analysis of Hot-Wire Measurements in Supersonic Turbulence,” AIAA Paper 88-423, 1988.
- <sup>30</sup>Smits, A. J. and Dussauge, J. P., *Turbulent Shear Layers in Supersonic Flow*, American Institute of Physics, 2nd ed., 2006.
- <sup>31</sup>Weiss, J., Knauss, H., and Wagner, S., “Experimental Determination of the Freestream Disturbance Field in a Short-Duration Supersonic Wind Tunnel,” *Experiments in Fluids*, Vol. 35, 2003, pp. 291–302.
- <sup>32</sup>Masutti, D., Spinosa, E., Chazot, O., and Carbonaro, M., “Disturbance Level Characterization of a Hypersonic Blow-Down Facility,” *AIAA Journal*, Vol. 50, No. 12, 2013, pp. 2720–2730.
- <sup>33</sup>Morkovin, M. V., “On Transition Experiments at Moderate Supersonic Speeds,” *Journal of the Aeronautical Sciences*, Vol. 24, No. 7, 1957, pp. 480–486.
- <sup>34</sup>Bull, M. K., “Wall-Pressure Fluctuations beneath Turbulent Boundary Layers: Some Reflection on Forty Years of Research,” *Journal of Sound and Vibration*, Vol. 190, No. 3, 1996, pp. 299–315.
- <sup>35</sup>Del Alamo, J. C. and Jimenez, J., “Estimation of Turbulent Convection Velocities and Corrections to Taylor’s Approximation,” *Journal of Fluid Mechanics*, Vol. 640, 2009, pp. 5–26.
- <sup>36</sup>Kim, J. and Hussain, F., “Propagation Velocity of Perturbations in Turbulent Channel Flow,” *Physics of Fluids*, Vol. 5, No. 3, 1993, pp. 695–706.
- <sup>37</sup>Choi, H. and Moin, P., “On the Space-Time Characteristics of Wall-Pressure Fluctuations,” *Physics of Fluids*, Vol. 2, No. 8, 1990, pp. 1450–1460.
- <sup>38</sup>Kistler, A. L. and Chen, W. S., “The Fluctuating Pressure Field in a Supersonic Turbulent Boundary Layer,” *Journal of Fluid Mechanics*, Vol. 16, 1963, pp. 41–64.
- <sup>39</sup>Fedorov, A. V., “Receptivity of a High-Speed Boundary Layer to Acoustic Disturbances,” *Journal of Fluid Mechanics*, Vol. 491, 2003, pp. 101–129.
- <sup>40</sup>Liepmann, H. W. and Roshko, A., *Elements of Gasdynamics*, John Wiley & Sons, Inc. New York, 1957.

Table 1. Freestream conditions for Mach 6 DNS of turbulent boundary layers.

$M_\infty$	$U_\infty(\text{m/s})$	$\rho_\infty(\text{kg/m}^3)$	$T_\infty(\text{K})$
5.86	870.4	0.0427	55.0

Table 2. Boundary layer properties at the station selected for the analysis of the pressure field ( $x_a = 57\delta_i$  for Case M6Tw076 and  $x_a = 80\delta_i$  for Case M6Tw025). The local boundary layer thickness  $\delta$  is approximately  $\delta \approx 1.8\delta_i$  for Case M6Tw076 and  $\delta \approx 2.6\delta_i$  for Case M6Tw025.

Case	$T_w(\text{K})$	$T_w/T_r$	$Re_\theta$	$Re_\tau$	$Re_{\delta_2}$	$\theta(\text{mm})$	H	$\delta(\text{mm})$	$z_\tau(\mu\text{m})$	$u_\tau(\text{m/s})$
M6Tw025	97.5	0.25	4650.7	465.8	2347.1	0.193	8.45	3.70	7.98	34.0
M6Tw076	300	0.76	9656.4	464.1	1782.8	0.969	13.6	24.4	52.6	45.0

Table 3. Grid resolution and domain size for Case M6Tw076.  $L_x$ ,  $L_y$ , and  $L_z$  are the domain size in the streamwise, spanwise, and wall-normal directions, respectively.  $\Delta x^+$  and  $\Delta y^+$  are the uniform grid spacing in the streamwise and spanwise directions, respectively, with the viscous length scale  $z_\tau = 52.6\mu\text{m}$  corresponding to the station selected for statistical analysis ( $x/\delta_i = 57$ ).  $\Delta z_{min}^+$  and  $\Delta z_{max}^+$  are the minimum and maximum wall-normal grid spacing for  $0 \leq z/\delta_i \leq 7$ .

Case	$N_x \times N_y \times N_z$	$L_x/\delta_i$	$L_y/\delta_i$	$L_z/\delta_i$	$\Delta x^+$	$\Delta y^+$	$\Delta z_{min}^+$	$\Delta z_{max}^+$
M6Tw076, Baseline	$1600 \times 800 \times 500$	58.7	15.7	39.7	9.64	5.14	0.51	5.33
M6Tw076, AI	$1920 \times 320 \times 500$	70.4	6.26	39.7	9.64	5.14	0.51	5.33
M6Tw076, AII	$2400 \times 480 \times 700$	58.7	6.26	39.7	6.43	3.43	0.51	3.55

Table 4. The disturbance field in the free stream for Case M6Tw025.

$u'_{rms}/\bar{u}$	$v'_{rms}/\bar{u}$	$w'_{rms}/\bar{u}$	$p'_{rms}/\bar{p}$	$\rho'_{rms}/\bar{\rho}$	$T'_{rms}/\bar{T}$
$2.45 \times 10^{-3}$	$1.64 \times 10^{-3}$	$3.26 \times 10^{-3}$	$3.53 \times 10^{-2}$	$2.52 \times 10^{-2}$	$1.01 \times 10^{-2}$
$(\rho u)'_{rms}/\bar{\rho}\bar{u}$	$T'_{t,rms}/\bar{T}_t$	$p'_{t,rms}/\bar{p}_t$	$(\partial u_i/\partial x_i)^2/\bar{\Omega}'_i\bar{\Omega}'_i$	$s'_{rms}/R$	
$2.31 \times 10^{-2}$	$3.23 \times 10^{-3}$	$1.13 \times 10^{-2}$	2985	$2.18 \times 10^{-4}$	
$\overline{u'p'}/u'_{rms}p'_{rms}$	$\overline{v'p'}/v'_{rms}p'_{rms}$	$\overline{w'p'}/w'_{rms}p'_{rms}$	$\overline{\rho'p'}/\rho'_{rms}p'_{rms}$	$\overline{T'p'}/T'_{rms}p'_{rms}$	
-0.845	-0.039	0.955	1.0	1.0	

Table 5. The disturbance field in the free stream for Case M6Tw076.

$u'_{rms}/\bar{u}$	$v'_{rms}/\bar{u}$	$w'_{rms}/\bar{u}$	$p'_{rms}/\bar{p}$	$\rho'_{rms}/\bar{\rho}$	$T'_{rms}/\bar{T}$
$1.31 \times 10^{-3}$	$1.04 \times 10^{-3}$	$2.05 \times 10^{-3}$	$2.01 \times 10^{-2}$	$1.43 \times 10^{-2}$	$5.78 \times 10^{-3}$
$(\rho u)'_{rms}/\bar{\rho}\bar{u}$	$T'_{t,rms}/\bar{T}_t$	$p'_{t,rms}/\bar{p}_t$	$(\partial u_i/\partial x_i)^2/\bar{\Omega}'_i\bar{\Omega}'_i$	$s'_{rms}/R$	
$1.35 \times 10^{-2}$	$1.93 \times 10^{-3}$	$6.48 \times 10^{-3}$	1131.2	$2.27 \times 10^{-3}$	
$\overline{u'p'}/u'_{rms}p'_{rms}$	$\overline{v'p'}/v'_{rms}p'_{rms}$	$\overline{w'p'}/w'_{rms}p'_{rms}$	$\overline{\rho'p'}/\rho'_{rms}p'_{rms}$	$\overline{T'p'}/T'_{rms}p'_{rms}$	
-0.632	-0.005	0.918	0.999	0.993	

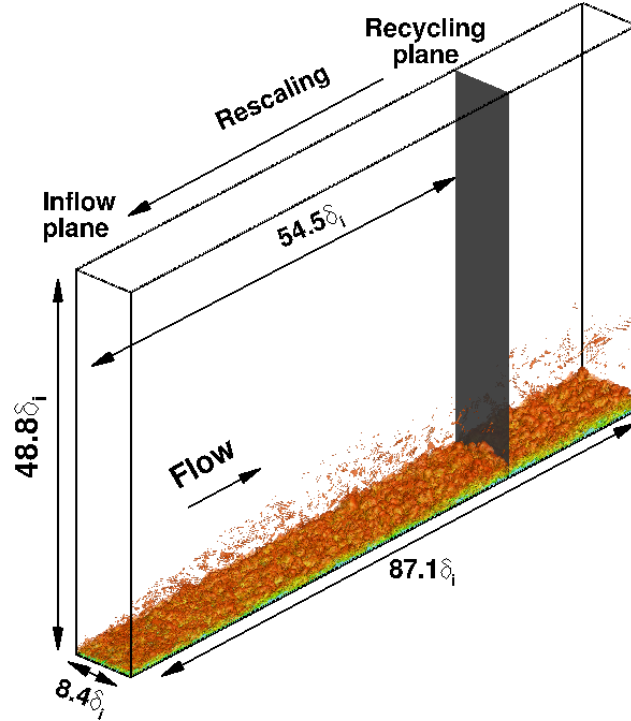


Figure 1. Computational domain and simulation setup for Case M6Tw025, which is also representative of the other case. The reference length  $\delta_i$  is the thickness of the boundary layer (based on 99% of the freestream velocity) at the inflow plane. An instantaneous flow field is shown in the domain, visualized by an iso-surface of the magnitude of density gradient,  $|\nabla\rho|\delta_i/\rho_\infty = 0.98$ , colored by the streamwise velocity component (with levels from 0 to  $U_\infty$ , blue to red).

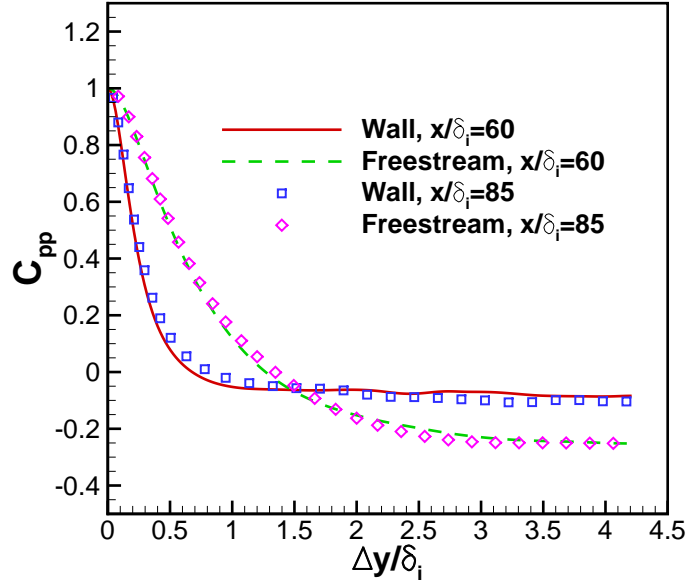


Figure 2. The correlation coefficient of pressure fluctuations as a function of spanwise separation at the wall ( $z/\delta = 0$ ) and in the freestream ( $z/\delta = 2.43$ ), at selected streamwise locations  $x = 60\delta_i$  and  $x = 85\delta_i$  for Case M6Tw025.

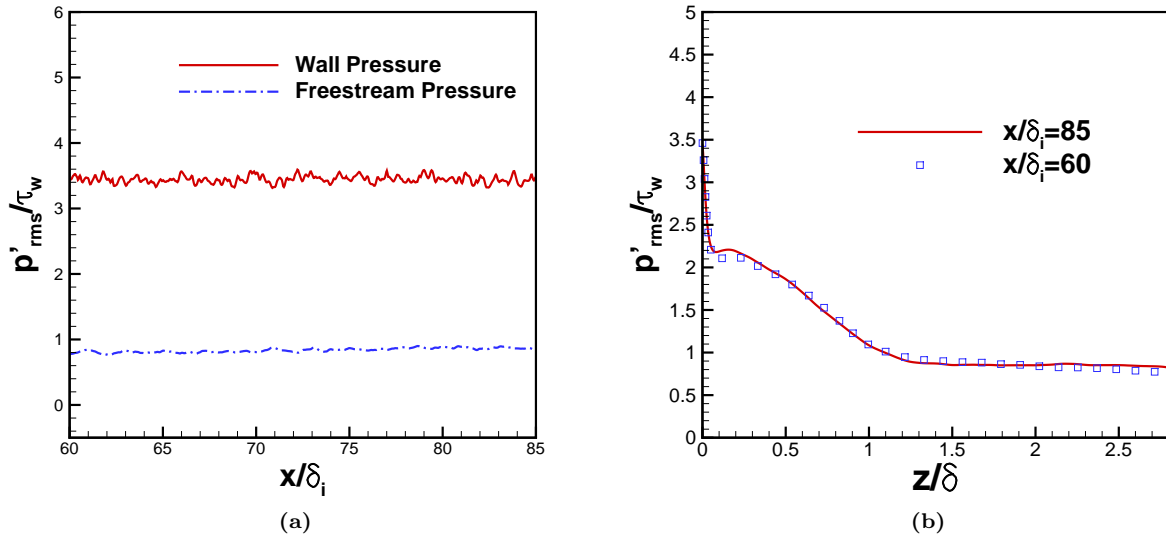


Figure 3. (a) Streamwise and (b) wall-normal distributions of the normalized rms pressure fluctuation in the downstream portion of the computational domain ( $60 < x/\delta_i < 85$ ) for Case M6Tw025. The freestream location is picked as  $z/\delta = 2.43$ .

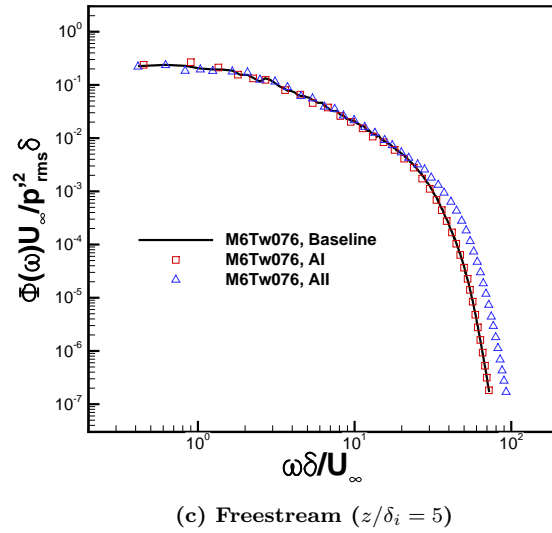
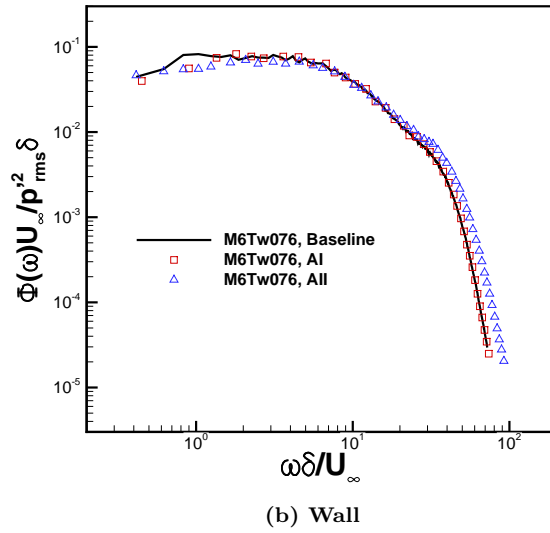
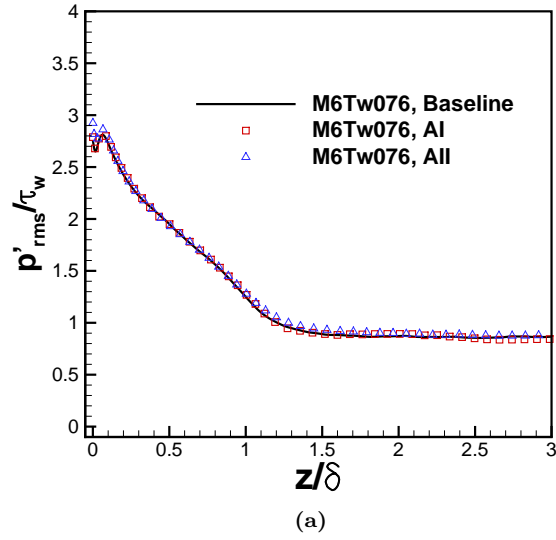


Figure 4. Comparison of (a) rms pressure fluctuation and (b,c) frequency spectra of pressure signal at the wall and in the freestream for DNS solutions based on varying domain size and grid resolutions. The DNS cases are listed in Table 3.

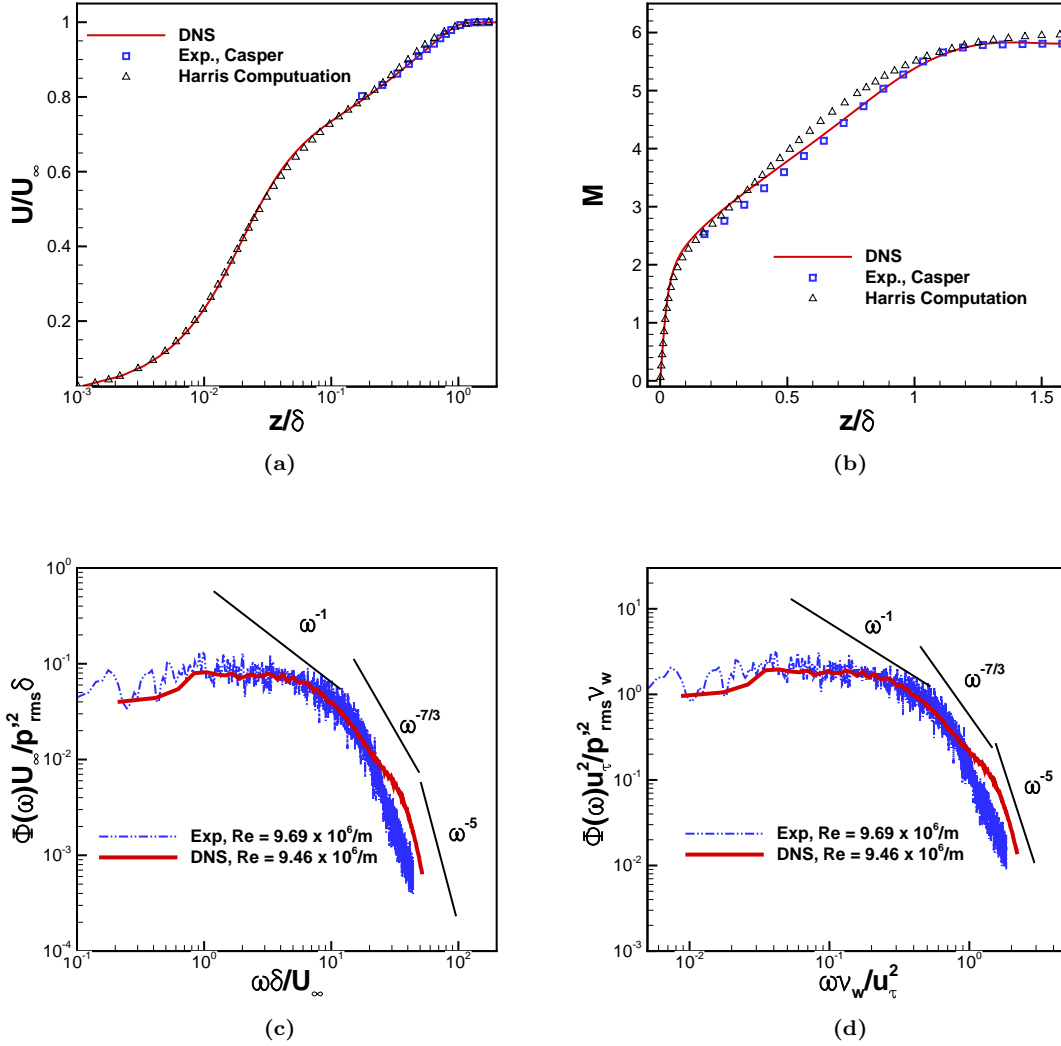


Figure 5. Comparison of DNS results (Case M6Tw076) with those of a Mach-5.8 turbulent boundary layer on the nozzle wall of the Boeing/AFOSR Mach-6 Quiet Tunnel under noisy-flow conditions ( $Re = 9.69 \times 10^6/m$ ,  $P_{t,\infty} = 965$  kPa,  $T_{t,\infty} = 429$  K). The wind-tunnel measurement and the calculation using Harris boundary-layer Code<sup>24</sup> were conducted by Katya Casper. (a) Mean velocity profile; (b) Mach number profile; (c) frequency spectrum in outer scale; (d) frequency spectrum in inner scale.

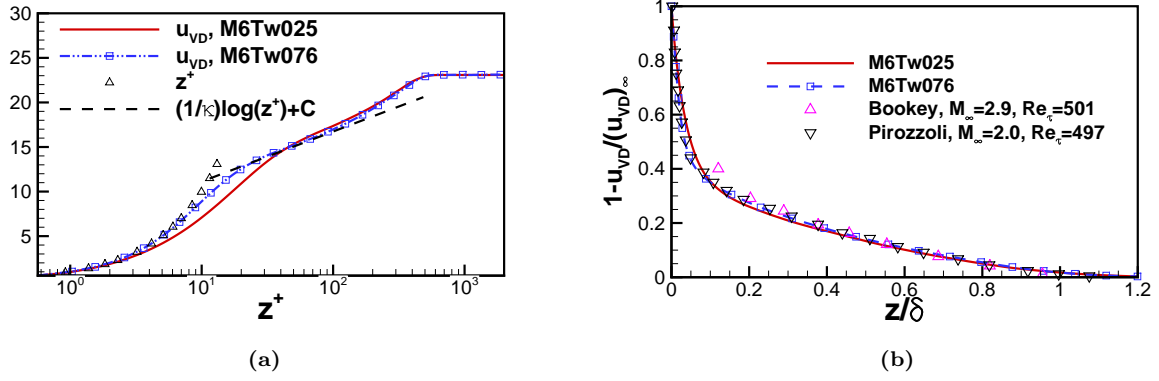


Figure 6. (a) van Driest transformed mean velocity profile ( $\kappa = 0.41$ ,  $C = 5.5$ ) and (b) van Driest transformed mean deficit velocity for Case M6Tw025. Symbols denote the DNS by Pirozzoli & Bernardini<sup>26</sup> at Mach 2,  $Re_\tau = 497$  (squares) and the experiment by Bookey et al.<sup>25</sup> at Mach 2.9,  $Re_\tau = 501$  (down-pointing triangles). The DNS cases are listed in Table 2.



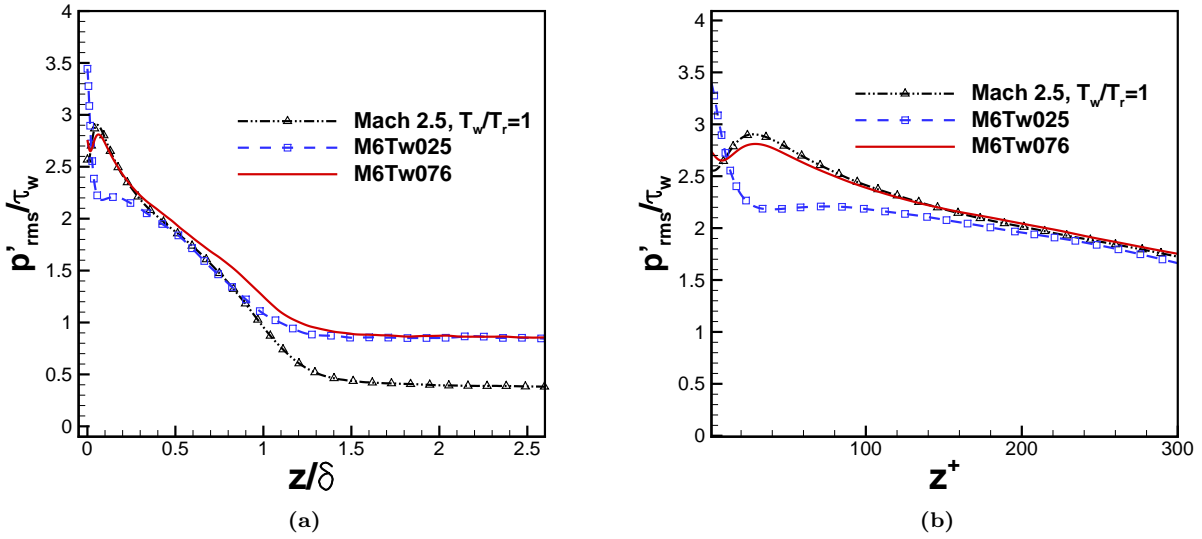


Figure 7. (a) Pressure fluctuation rms normalized by the wall-shear stress for the present DNS and the Mach 2.5 DNS by Duan et al.<sup>14</sup> in outer and inner scales.

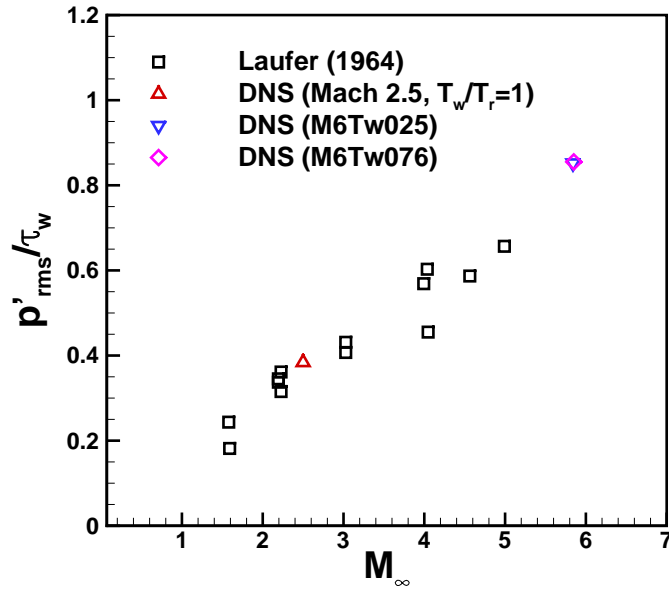
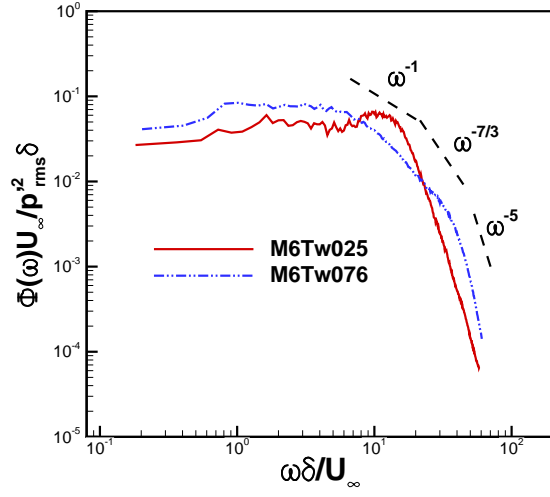
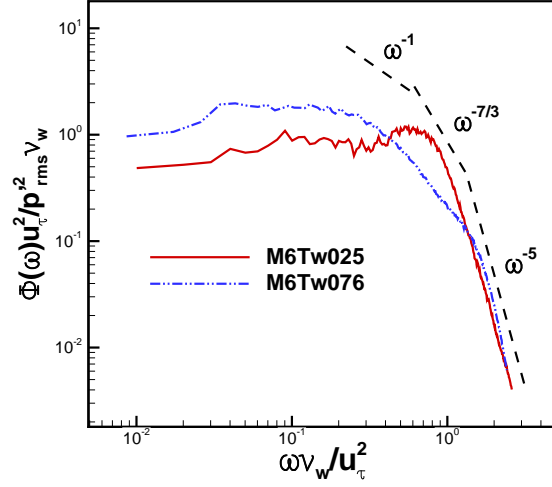


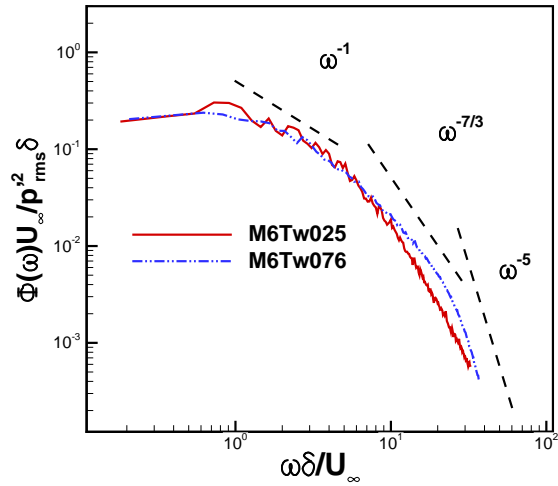
Figure 8. Intensity of freestream pressure fluctuation compared with the experiments by Laufer.<sup>5</sup>



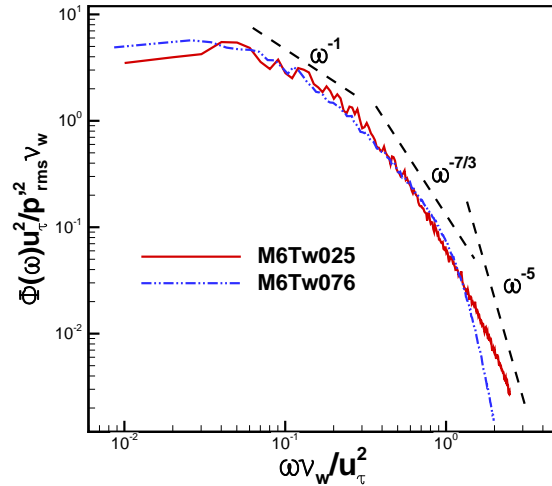
(a) Wall



(b) Wall



(c) Freestream



(d) Freestream

Figure 9. Comparison of power spectral density at the wall and in the freestream ( $z/\delta = 2.43$ ) for Cases M6Tw025 and M6Tw076.

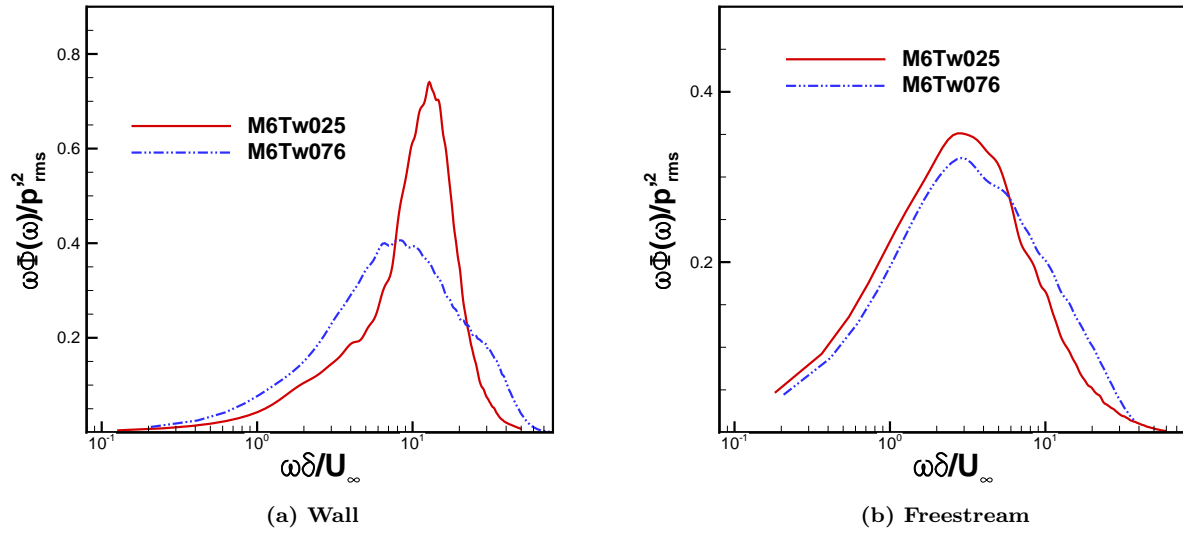


Figure 10. Comparison of pre-multiplied power spectral density at the wall and in the freestream ( $z/\delta = 2.43$ ) for Cases M6Tw025 and M6Tw076.

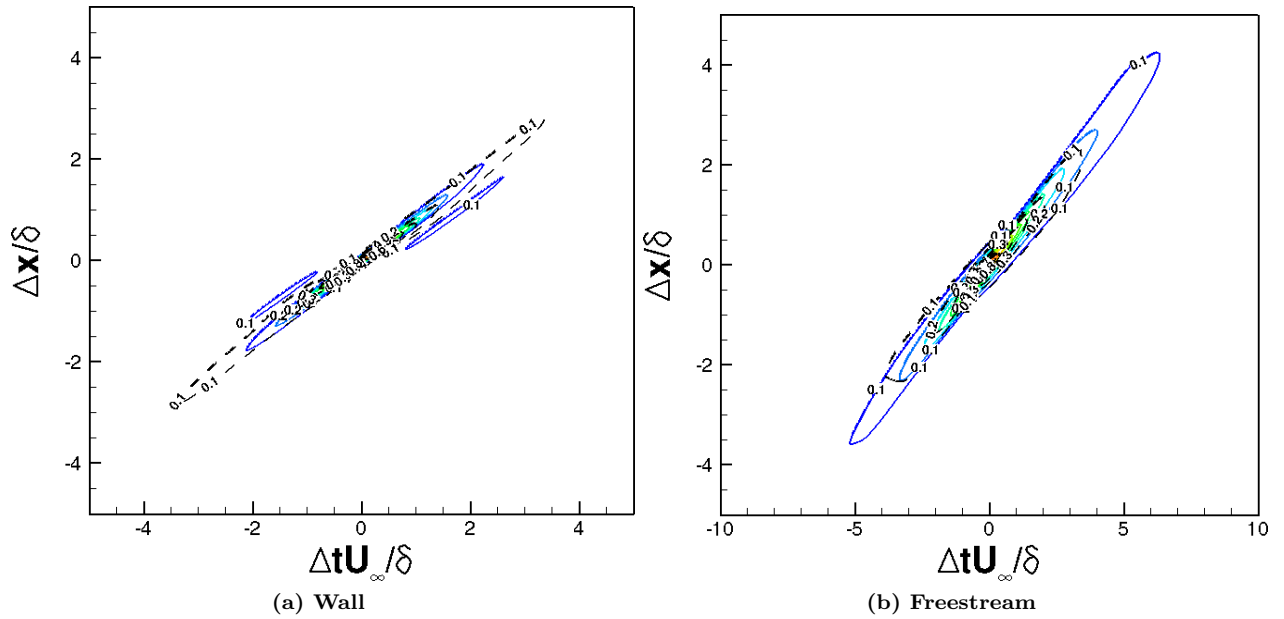


Figure 11. (a) space-time correlation at the wall and in the freestream ( $z/\delta = 2.43$ ). The solid contours are for Case M6Tw025 and the dashed contours are for Case M6Tw076.

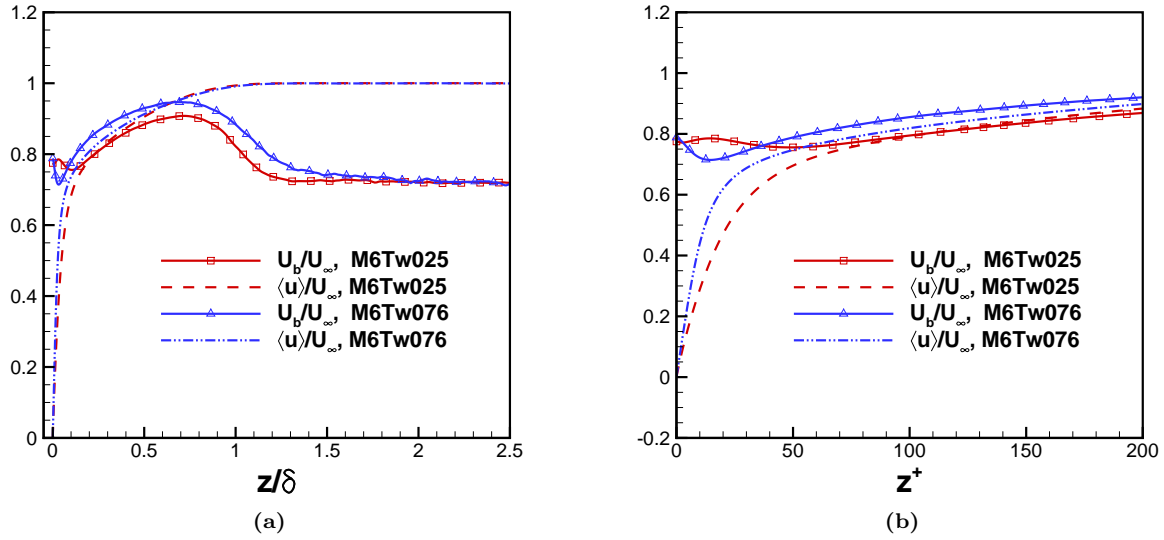


Figure 12. Bulk propagation speed of pressure fluctuations as a function of wall-normal distance in (a) outer and (b) inner units.

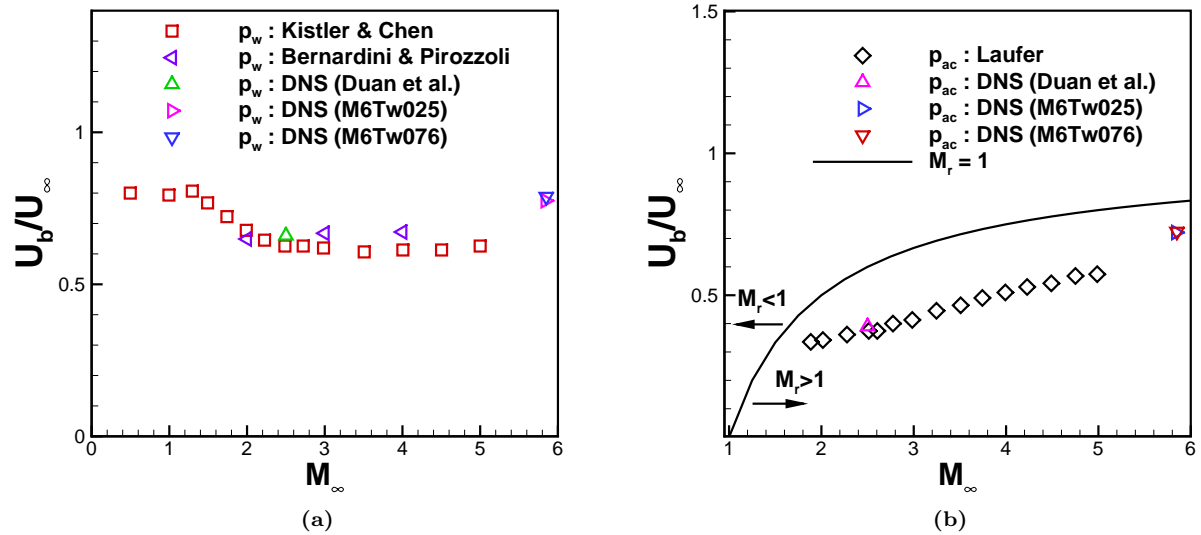


Figure 13. Bulk convection speeds of the pressure fluctuation as a function of freestream Mach number: (a) at the wall; (b) in the freestream. Symbols: *squares*, Kistler & Chen;<sup>38</sup> *Left triangles*, Bernardini & Pirozzoli;<sup>27</sup> *diamonds*, Laufer;<sup>5</sup> *deltas*, Duan et al.;<sup>14</sup> *right triangles*, Present DNS, Case M6Tw025; *gradients*, Present DNS, Case M6Tw076. Lines:  $M_r = 1$ .

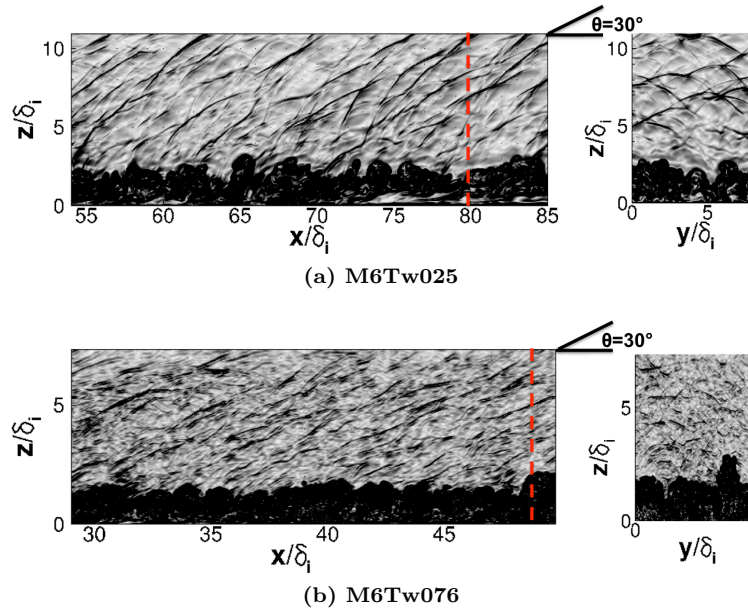


Figure 14. Numerical schlieren image based on instantaneous flow field for Cases M6Tw025 and M6Tw076. Contour levels are selected to emphasize disturbances in the freestream.  $\theta$  is the angle between the wave front and the flow direction; and the vertical dashed line indicates the streamwise location of the selected spanwise–wall-normal plane visualized in the right panel.